Emergence of a low-viscosity channel in subduction zones through the coupling of mantle flow and thermodynamics

Laura Baker Hebert *, Paula Antoshechkina, Paul Asimow, Michael Gurnis

California Institute of Technology; Pasadena CA 91125, United States

ARTICLE INFO

ABSTRACT

We use a petrological model (pHMELTS), coupled with a 2D thermal and variable viscosity flow model (ConMan), to describe and compare fundamental processes occurring within subduction zones. We study the thermal state and phase equilibria of the subducting oceanic slab and adjacent mantle wedge and constrain fluid flux. Using a Lagrangian particle distribution to perform thousands of thermodynamically equilibrated calculations, the chemical state of the domain is continuously updated. Compositionally and thermally dependent buoyancy and viscosity terms provide a consistent linkage between the effect of water addition to and flow within the mantle wedge. We present seven model cases that span normal ranges in subducting slab age, convergence velocity, and slab dip angle. In all models, the coupling between chemistry and dynamics results in behavior previously unresolved, including the development of a continuous, slab-adjacent low-viscosity channel (LVC) defined by hydrous mineral stability and higher concentrations of water in nominally anhydrous minerals (NAM). As the LVC evolves to fluid saturation, slab-derived components are able to migrate vertically upwards to the water-saturated solidus, forming a melting region that bounds the top of the LVC. The LVC develops due to fluid ingress into the mantle wedge from the dehydrating slab, and can be responsible for slab decoupling, large-scale changes in the wedge flow field, and a mechanism by which hydrated slab-adjacent mantle material can be transported to the deep mantle. Varying model parameters indicates that slab age and slab dip angle exert primary control over LVC shape and thickness, due to changing fluid release patterns within the slab. Younger slabs tend to have thinner, more uniform LVCs, while older slabs tend to have a thinner LVC at shallow depths with a large increase in LVC thickness at ~ 100 km depth. Slab convergence velocity appears to have a secondary role in controlling LVC shape.

© 2008 Published by Elsevier B.V.

1. Introduction

Complete understanding of subduction requires a model that accounts for complex interactions between chemical and dynamic features of the system. Studies focusing on force balance or chemistry, using results from one to infer behaviors in the other, have reached broad conclusions regarding the manner of hydration of the mantle wedge and melting beneath the arc (Peacock, 1990; Davies and Stevenson, 1991; Iwamori, 1998; Schmidt and Poli, 1998; Arcay et al., 2005; Van Keken et al., 2002). However, when subduction processes are addressed through a coupled geophysical and geochemical model, emphasizing interdependent contributions, more detailed interpretations may be made. The input of dynamical quantities such as flow field and thermal structure to thermodynamic calculations, which output chemically-governed quantities such as melt fraction, compositional buoyancy, viscosity, water speciation, and latent heat contributions,

forms an essential loop that couples chemical and physical processes. Indeed, it is this strong coupling that presents insights into the subduction system on a fundamental level.

A particular part of the subduction system where coupling between geophysical and geochemical processes is important is the mantle wedge adjacent to the slab. There is general agreement that water-rich fluids enter the overlying mantle as the slab descends and that the pressure–temperature path, chemical composition, and phase equilibria within the dehydrating slab determine the locations of fluid release (Schmidt and Poli, 1998). This fluid phase interacts with the overlying mantle, hydrates the peridotite and, where temperature is sufficient, induces water-fluxed melting (Tatsumi and Eggins, 1995). However, the mechanism of wedge hydration and the pathways by which fluids reach the sites of melting remain speculative (Iwamori, 1998; Schmidt and Poli, 1998). Previous modeling has specifically addressed the role of water in the subduction system together with dynamical considerations, emphasizing the role of hydrous minerals as transport agents and/or sources of water and using phase diagrams for the peridotite solidus (Davies and Stevenson, 1991; Iwamori, 1998; Arcay et al., 2005). These classic studies do not account for changing peridotite phase relations due

---

* Corresponding author. Present address: University of Maryland; College Park MD 20742, United States. Fax: +1 301 314 7970.
E-mail address: lhebert@geol.umd.edu (L.B. Hebert).

to melt extraction, for water partitioning into nominally anhydrous minerals (NAM), or for variable viscosity flow in the wedge. Recent investigations introduced the potential importance of NAM in melt initiation, the water budget and subduction zone dynamics, specifically water-weakening (Hirth and Kohlstedt, 1996; Mei and Kohlstedt, 2000; Hauri et al., 2006). A low-viscosity mantle wedge has been shown to substantially affect the force balance in a subduction zone, leading to observable signals in the topography, state of stress, gravity, and geoid (Sleep, 1975; Billen and Gurnis, 2001; Hebert and Gurnis, in press) and potentially resolving the over-prediction of back-arc basin depths by several kilometers (Billen and Gurnis, 2001). The viscosity of the wedge may be at least a factor of 10 smaller than the surrounding mantle lithosphere and asthenosphere (Billen and Gurnis, 2001), consistent with estimates from seismic dissipation (Karato and Jung, 1998) and rock deformation experiments (Hirth and Kohlstedt, 1996).

While the importance of a localized low-viscosity region has been evaluated, the mechanism by which it develops and its detailed geometry have yet to be considered. This study aims to improve upon previous modeling with an internally consistent treatment, including water in NAM and emphasizing the origination and development of hydration features in the mantle wedge. Towards this end, we present the coupled geochemical and geodynamic model GyPSM-S (*G*eodynamic and *P*etrological *S*ynthesis *M*odel for *S*ubduction).

2. Model formulation

2.1. Component programs

The two primary components within the GyPSM-S computational scheme are (1) ConMan, a two-dimensional thermal and variable viscosity numerical flow model (King et al., 1990), and (2) pHMELTS, a thermodynamic energy minimization algorithm that can calculate water partitioning into NAM (Ghiorso and Sack, 1995; Asimow et al., 2004; Smith and Asimow, 2005).

ConMan solves equations for incompressible buoyant viscous flow using the finite element method (FEM) in two dimensions. The dynamics are controlled by conservation equations of mass, momentum, and energy, with the Boussinesq approximation. The non-dimensional equations for mass and momentum are:

$$\nabla \cdot v' = 0 \tag{1}$$

and

$$\nabla P' - \nabla \cdot (\eta' \nabla v') = RaT'\hat{k}, \tag{2}$$

where v' is dimensionless velocity, T' is dimensionless temperature, P' is dimensionless pressure, η' is dimensionless viscosity, and k is a unit vector in the direction of gravity. The dimensionless Rayleigh number combines all the material properties:

$$Ra = \frac{g\alpha\rho\Delta T d^3}{\kappa\eta}, \tag{3}$$

where g is acceleration due to gravity, α is the coefficient of thermal expansion, ΔT is vertical temperature drop, d is depth of the box (Table 2), κ is thermal diffusivity, and η is dynamic viscosity (Table 1). A penalty formulation is used to enforce incompressibility in the solution of the momentum equation (King et al., 1990).

The effects of latent heats of melting, hydration, and dehydration are better evaluated in pressure-entropy space, where an isentropic calculation can result in an increase or decrease in temperature, depending on melting or crystallization. Consequently, we

have modified the energy equation to advect entropy instead of temperature:

$$\frac{\partial S'}{\partial t'} = -v' \cdot \nabla S' + \frac{C'_p}{T'}(\nabla^2 T'), \tag{4}$$

where S' is dimensionless entropy, C'_p is dimensionless heat capacity, and t' is dimensionless time. A streamline upwind Petrov–Galerkin method (Brooks and Hughes, 1982) is used to solve Eq. (4).

The viscosity law is both temperature and composition dependent, as influenced by water in olivine (Hirth and Kohlstedt, 1996):

$$\eta' = \frac{\eta}{\eta_0} = \exp\left[\frac{Q}{RT_0} * \left(\left(\frac{T_0}{T}\right) - 1\right)\right] * \left(\frac{XH_2O}{XH_2O_{crit}}\right)^{-1} \tag{5}$$

where $XH_2O > XH_2O_{crit}$, η_0 is reference viscosity, Q is activation energy, R is the gas constant, T_0 is the model reference temperature, XH_2O is water content in olivine, and XH_2O_{crit} is a critical value for water weakening (Table 1). The law was determined empirically from experiments on dislocation creep of hydrated olivine aggregates (Hirth and Kohlstedt, 2003) and is intentionally simple, so that it will extrapolate well to pressures, temperatures, and water contents well outside current experimental bounds. The viscosity of the thermal lithosphere and the slab depends on temperature and has a maximum value of $10^3 \times \eta_0$ for the coldest regions.

The initial and boundary conditions are summarized in Fig. 1. The velocity of the subducting slab and subjacent material is kinematically imposed (Table 2). The velocity boundary conditions on the left-hand side and the base of the wedge domain are taken from an analytical solution for corner flow (Eq. 4.8.23: Batchelor, 1967) while velocities within the wedge itself are computed dynamically. The top surface is isothermal and the thermal age of the down-going slab determines the temperature (and entropy) of incoming slab material throughout the calculation. The rigid over-riding plate and prescribed potential temperature define the conductive geotherm on the opposite sidewall (using the definition and calculation method for lithospheric thickness from McKenzie and Bickle, 1988) and a pHMELTS-calculated adiabatic gradient and entropy profile completes the imposed boundary conditions. This explicit treatment of the thermal boundary layer discourages artificial melting of the peridotite immediately upon entering the model domain.

The underlying thermodynamic model behind pHMELTS is pMELTS (Ghiorso et al., 2002). The pHMELTS calculation uses trace element partitioning to distribute water between the system (melt, pure vapor,

Table 1
Model parameters

Parameter	Value	Units
T_0	1773	K
ΔT	1500	K
Ra	1.6E+04	*
H_0	1.0E+21	Pa s
R	8.31	J/K mol
XH_2O_{crit}	110	ppm
Q	500	kJ/mol
N	3 (a)	* (1)
C	2.7E+02 (a)	*
η_W	1.0E+00 to 1.0E−04 (b)	Pa s
d_m	1.0E−03	m
κ	1.0E−06	m²/s
α	4.0E−05	K⁻¹
g	10.0	m/s²
MINF	0.005	* (2)
Adiabatic gradient	0.7	°C/km

*Indicates non-dimensional quantity.
(a) Wark et al. (2003); (b) Audetat and Keppler (2004).
(1) Experimental investigation of natural systems indicates that the pore geometry may be anisotropic (Zimmerman et al., 1999); differing significantly from an idealized case in which flow occurs in an isotropic network of cylindrical pores of uniform size in natural systems such that n=3 (Wark et al., 2003).
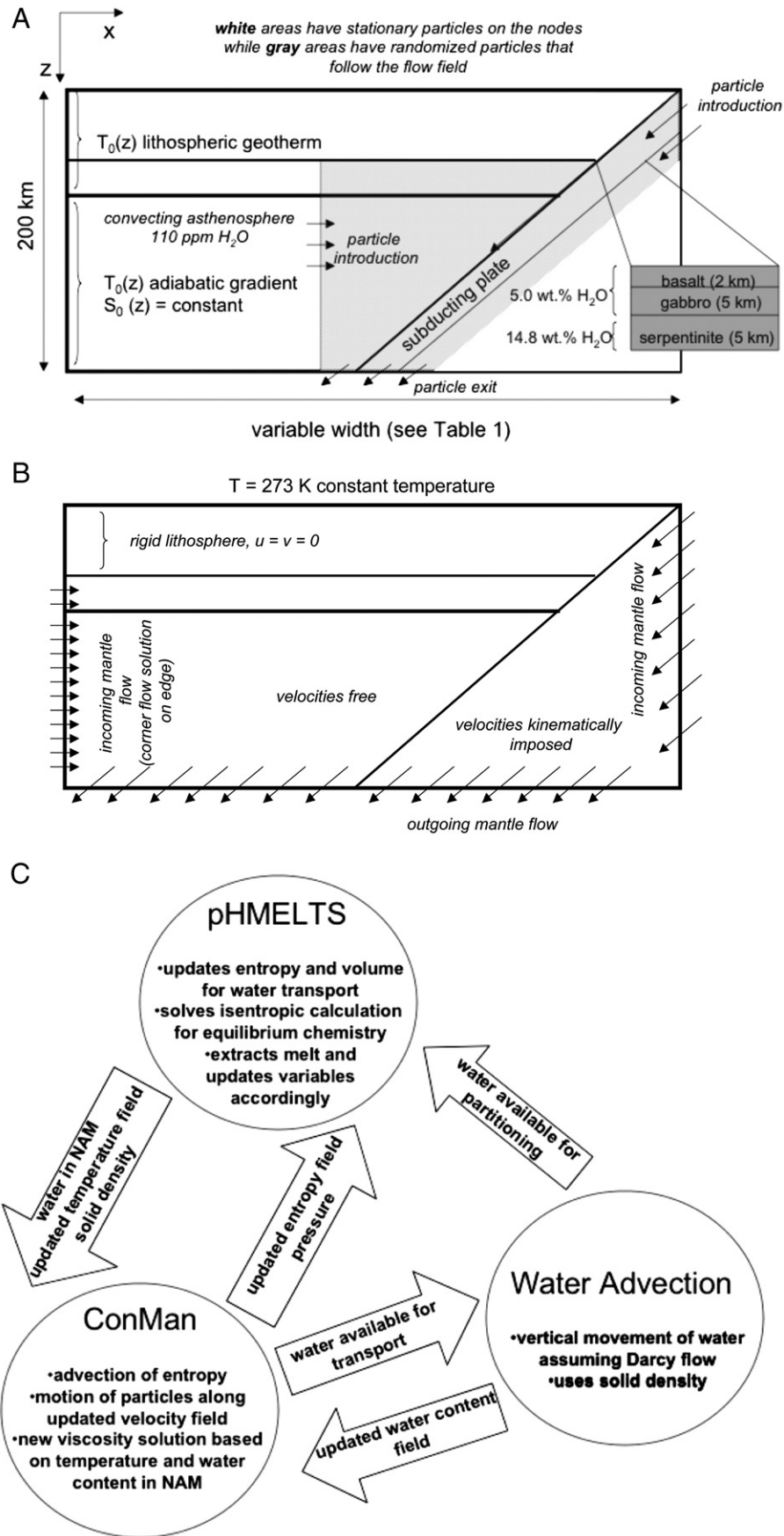(2) A small but finite residual porosity acts to stabilize the pHMELTS calculation.

Fig. 1. (A) Initial conditions, (B) boundary conditions imposed within the GyPSM-S model domain, and (C) computational organization and data flow of the GyPSM-S model. See text for details.

Table 2
A summary of subduction zone model parameters

approximate subduction region	Central Costa Rica	Southeastern Costa Rica	Northern Izu-Bonin	Northern Mariana	Additional Model 1	Additional Model 2	Additional Model 3
abbreviation	CCR	SCR	NIB	NMAR	ADD1	ADD2	NIB
latitude	~8–11° N	~8–11° N	~32° N	~23° N	N/A	N/A	N/A
longitude	~275–277° E	~276–278° E	~135–143° E	~143–145° E	N/A	N/A	N/A
rate of convergence (mm/yr)	87 (a)	90 (a)	50 (b)	47.5 (b)	87.00	50.00	50.00
slab dip (degrees)	45 (a)	30 (a)	45 (b)	60 (b)	45	45	45
slab thermal age (Ma)	18 (a)	15 (a)	135 (b)	165 (b)	135	18	135
rigid lithospheric thickness (km)	50 (a)	50(a)	32(c)	32(c)	50	50	50
thermal lithospheric thickness (km)	88	88	66	66	88	88	88
dimensional grid resolution (z,x)	2.0 km, 2.0 km	2.0 km, 3.4641 km	2.0 km, 2.0 km	2.0 km, 1.1547 km	2.0 km, 2.0 km	2.0 km, 2.0 km	2.0 km, 2.0 km
dimensions of model domain (z,x)	200 km, 400 km	200 km, 692.8 km	200 km, 400 km	200 km, 230.9 km	200 km, 400 km	200 km, 400 km	200 km, 400 km

(a) Peacock et al. (2005); (b) Stern et al. (2003); (c) Peate and Pearce (1998).
The computational grid consists of 2×10^4 uniformly sized bilinear quadrilateral elements: 100 in the vertical direction and 200 in the horizontal direction (20 301 Eulerian nodes). All numerical experiments use the same number of elements, and as such the different model grids have slightly different resolutions from one to another, as the width of the model domain varies among experiments.

or hydrous minerals) and a hidden reservoir within the NAM. Estimates of water solubility in olivine are from Mosenfelder et al. (2006). Bulk density is computed by pHMELTS from the equations of state of the constituent phases and the equilibrium phase assemblage and is a function of temperature, pressure, and composition. In regions outside the calibrated pressure–temperature range of pHMELTS, or on rare occasions when pHMELTS fails to converge, we use a scaled-down version of the algorithm in which the system is not fully re-equilibrated: water is partitioned between existing phases (including hydrous phases and NAM; usually excluding liquid) but only fluid can join the assemblage. At pressures above the pHMELTS maximum, we fit a Birch–Murnaghan equation of state for the *solid* phases so that the transition to the polynomial expression (Berman, 1988) normally used is continuous in volume and its first derivatives.

The calibration of pHMELTS does not encompass the full spectrum of slab lithologies; non-lherzolite slab lithologies refer to phase diagrams (Hacker et al., 2003) for dehydration reaction locations within pressure–temperature space. Alternative solvers use a heat-capacity polynomial formulation for entropy (Berman, 1988) with pMELTS-calculated end-member parameters, in conjunction with an equation of state for water (Pitzer and Sterner, 1994). We use the Clapeyron equation together with estimates of volume and entropy for solids (Berman, 1988; Hacker and Abers, 2004) and for fluid (Pitzer and Sterner, 1994) to ascertain the amount of free water liberated from the slab as univariant reactions are met. This treatment of isentropic slab dehydration accounts for the release of fluid over a finite pressure interval, approximating a continuous reaction.

2.2. Code coupling and tracer particles

The Adiabat_1ph interface to pHMELTS (Smith and Asimow, 2005) automates calculations using scripts to invoke subroutine versions of the (pH)MELTS program. GyPSM-S uses an extended version of Adiabat_1ph that includes the alternative solvers for slab lithologies, and is optimized for parallel processing. The component programs are executed and quantities such as temperature, entropy, volatile content in NAM, and water content passed in a loop structure (Fig. 1C) until the model reaches a state independent of its initial conditions. A network of ~4×10^4 Lagrangian particles, acting as chemical tracers, provide iterative feedback and are advected within ConMan using a predictor-corrector method (Sidorin and Gurnis, 1998); for one convective overturn (here about twice the residence time of a particle), the particles accumulate a spatial error $O(10^{-5})$. Four particles per element are randomly introduced within the area of interest and one particle per node is used in rigid regions or where bulk composition is unaffected by melting or fluid flux. This particle distribution maximizes computational efficiency and minimizes errors due to interpolation and boundary interference.

Particles within the model are assigned one of three compositional tags: (i) an initial depleted peridotite composition (Workman and Hart, 2005), solved using pHMELTS, (ii) hydrated altered oceanic crust (AOC) within the slab, and (iii) hydrated lithospheric serpentinite also within the slab (Fig. 1A). A serpentinite layer has been observed in Alpine ophiolites (Rüpke et al., 2004; Scambelluri et al., 2004) and seafloor exposures and is presumably formed by fluid introduction at the ridge crest or along normal faults occurring during plate bending (Ulmer and Trommsdorf, 1995). We do not include a sediment layer, assuming that most sediment water is lost to compaction early in slab descent (Rüpke et al., 2002). In selecting a single depleted mantle composition, we are not specifically accounting for the range of source compositions presumably encountered within subduction zone wedges, which can include depletion due to extraction of melt at a back-arc, or larger-scale mantle source variations. There is no K_2O included, which effectively suppresses formation of mica within pHMELTS, but results in a more realistic melt productivity. Equilibration of the original peridotite composition, mass-normalized to 100.0 g, occurs at 3.3 GPa, 1424.56 °C and f_{O_2}=NNO, which is then used as the starting composition within the pHMELTS algorithm. While mineral-melt trace element partitioning is included, pHMELTS cannot currently calculate trace elements within the fluid phase itself, making it impossible to directly include the fluid-mobile trace element composition of the slab lithologies in the fully-coupled experiments. Supplemental modeling done independently using GyPSM-S results is required to address this (Hebert et al., in prep.).

To maintain a uniform particle density, new particles are added (type depending on position) as older particles are advected out of the model domain (Fig. 1A). At every iteration, each particle is associated with an Adiabat_1ph equilibrium calculation with two-way interpolations at each timestep to pass information between components. The particle-to-node step uses a triangle-based linear interpolation scheme for smoothly-varying quantities like temperature, and an area-weighted bilinear scheme for available fluid. This combination minimizes errors in regions of high thermal gradients, namely in the wedge corner and along the slab interface, whilst conserving fluid mass. The node-to-particle step uses an area-weighted bilinear interpolation method. Slight numerical diffusion, due to interpolation, results in overall cooling of tens of degrees over the model duration concentrated in areas of high thermal gradients.

Initially, ConMan is run independently, using temperature-dependent viscosity, until a quasi-steady-state thermal structure is achieved; this becomes the thermal initial condition for coupled calculations. Particles are assigned an initial temperature after adjustment for the adiabatic gradient within the convecting portion of the mantle. The first set of Adiabat_1ph calculations is isothermal; inputs being temperature and pressure, and outputs being entropy, water content in NAM, melt fraction and composition, free fluid

content, trace element abundances, solid phase mode and mineral compositions, and melt and solid density. Each subsequent Adiabat_1ph calculation is isentropic, with entropy input and temperature output. At each ConMan timestep, the chemical information is returned to the FEM, influencing the viscosity and energy fields; key variables are updated accordingly. Particles move with the updated velocity field, giving a new pressure-entropy state that is sent to the next set of pHMELTS calculations. At each iteration, we assume that chemical equilibrium between the fluid and the solid matrix is attained. The total duration of the coupled computations in dimensional model time are typically two to five million years. This is sufficient to approach a state independent of initial conditions, judged by the complete progression of original particles through the model domain.

We employ a near-fractional melting scheme, such that after every iteration all but a small residual melt porosity (MINF, Table 1) is instantaneously removed. As the equations governing the finite element calculation assume incompressibility and single-phase flow, we do not allow the removed melt to interact with the remaining solid residue (amounting to an assumption of perfect chemical isolation of migrating melts), which negates the possibility of increases in temperature due to crystallization of extracted melt. Melt extraction depletes the residue, requiring that pHMELTS tracks the changing bulk composition of each particle. The residue, plus any residual liquid, is renormalized to 100.0 g of material so that the extensive quantities calculated by pHMELTS (such as entropy and volume) can be readily incorporated into ConMan, which deals with intensive quantities (such as density).

2.3. Water migration

The hydrated slab is progressively dehydrated as it moves deeper into the mantle through increasing temperatures and pressures. We account for the movement of entropy with the fluid phase and we assume that the initial state of the slab is water-saturated, resulting in an immediate flux of water into the wedge. The fluid is advected by Darcy's law, taking into account the estimated domain permeability:

$$\overline{v}_{water} - v_{solid} = \frac{k_\varphi g \Delta\rho}{\varphi \eta_W} \tag{6}$$

and

$$k_\varphi = \frac{d_m^2 \varphi^n}{C}, \tag{7}$$

where k_φ is permeability, d_m is the characteristic spacing of transport tubules (on the order of grain size), φ is mean fluid fraction, $\Delta\rho$ is density difference between fluid and solid, η_W is fluid viscosity, n is a constant parameter indicating the type of pore geometry, and C is a geometrical constant (Table 1). We consider a range of potential fluid velocities to assess the impact on the model results.

2.4. Model input parameters

To evaluate the role of changing physical characteristics in the thermal and chemical development of the LVC, we have varied subduction parameters among seven models, spanning globally significant ranges of convergence velocities (47.5–90 mm/yr), slab dip angles (30–60°), and slab thermal structures (incoming plate age 15–165 Ma) (Table 2). Four of the models are applicable to two geographical regions: (i) the Costa Rica–Nicaragua segment of the Central American subduction zone and (ii) the Izu-Bonin–Mariana subduction zone.

At the Central American subduction zone, relatively young lithosphere (15–25 Ma) of the Cocos Plate subducts beneath the Caribbean Plate (Peacock et al., 2005). Convergence rate increases slightly towards the southeast, but the primary difference between the Central Costa Rican (CCR) and Southeastern Costa Rican (SCR) models is slab dip, which changes from 45° to 30°, respectively. The Izu-Bonin–Mariana subduction zone involves relatively mature lithosphere of the western Pacific Plate subducting beneath the eastern Philippine Sea Plate (Stern et al., 2003), allowing us to evaluate the effects of a significantly older slab and a slower convergence rate. The slab dip also varies from 45° in the Northern Izu-Bonin (NIB) model to 60° in the Northern Marianas (NMAR) model. Model ADD1 addresses fast subduction of an older plate, while ADD2 is a slow-subducting young plate. Model ADD3 resembles model NIB but with a thicker overlying lithosphere. All ADD models have slab dips of 45°, permitting a direct comparison of slab age and slab convergence velocity with models CCR and NIB.

3. Model results

3.1. Development of the low-viscosity channel and controls on its shape

For a young, moderately fast subducting plate, we summarize the process of slab-adjacent mantle wedge hydration (Fig. 2). In the early stages, the majority of the shallow water release (<100 km) is due to reactions within the AOC layer (jadeite lawsonite blueschist → lawsonite amphibole eclogite, lawsonite amphibole eclogite → amphibole eclogite, and amphibole eclogite → zoisite eclogite) (Hacker et al., 2003). Reactions within the serpentinite layer account for fluids coming from ~110 km depth (chlorite brucite serpentinite → serpentine chlorite dunite; lithologic descriptions from Hacker et al., 2003) and from ~170 km depth (chlorite harzburgite → garnet harzburgite) (Hacker et al., 2003). As the initial fluid transient dissipates, the primary sources of fluid are within the AOC (60–80 km depth) and at approximately 140 km depth within the serpentinite layer. The increase in the water content of NAM within 25 km of the slab (Fig. 2C) creates a strong reduction (10^1 to 10^2 ×) in wedge viscosity (Fig. 2D). The low-viscosity zones extend into a continuous layer that is entrained downwards in the slab-dominated velocity field. Ultimately, the low-viscosity region extends from ~50 km depth to the model base (200 km) and results in a non-uniform low-viscosity channel (LVC) (Fig. 2F). The difference in hydration between the ambient mantle wedge and the LVC increases with depth, leading to a strong lateral variation in viscosity. This model has no deeper fluid release, so the LVC thickness at 200 km is mainly due to advection of hydrated material from lower pressures, with slight thinning relative to parts of the LVC directly above fluid sources. The flow field within wedge changes with the development of the LVC (compare streamlines in Fig. 2A and E) such that there is a stronger component of upward flow across the boundary between the nominally anhydrous mantle wedge and the hydrated LVC.

In addition to NAM, hydrous phases are present within the hydrated region of the slab-adjacent wedge. Amphibole appears at pressures below 2.1 GPa and chlorite is stable below ~1000 K from 2.0 GPa to ~5.3 GPa (Pawley, 2003; Grove et al., 2006; Smith et al., 2007), leading to a continuous hydrous phase layer within the wedge above the slab surface. Small amounts of deep chlorite (>5.3 GPa) are an artifact of pHMELTS not including a higher-P hydrous phase such as Mg-sursassite or phase A.

A localized region of hydrous (8–15 wt.% H_2O) melt production is promoted by water-fluxing. Instantaneous low-degree fractional melts bound the top of the LVC (water-saturated solidus). As melting initiates, water partitions strongly into the melt phase so the fluid phase becomes undersaturated and disappears, preventing further transport of water and additional flux melting. The melting region is therefore thin and is restricted to the top of the LVC, displaced significantly from the slab–wedge interface. Indeed, melt initiation constrains the geometry of the hydrated region as a comparison
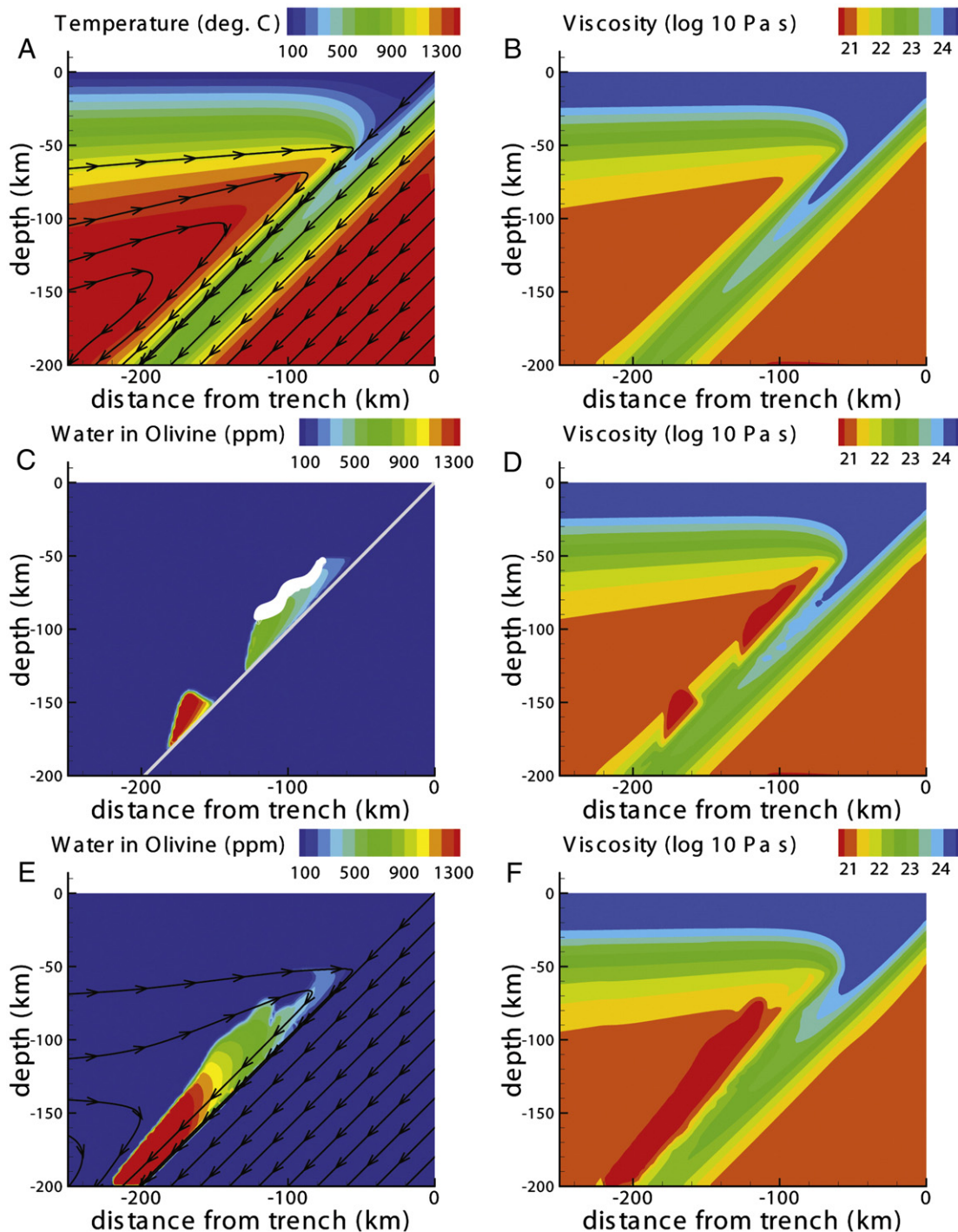
Fig. 2. Development of LVC for model CCR: (A) initial thermal structure and streamfunction (with arrows showing direction of flow), resulting from an uncoupled ConMan calculation approaching steady-state; (B) initial viscosity structure, calculated immediately after the first coupled iteration with pHMELTS such that the water content of the ambient mantle is reflected in the viscosity structure as well as temperature-dependent contributions; (C) increase in water in olivine above the ambient background as fluid from the dehydrating slab rises into the wedge and then reacts with the peridotite to form hydrous phases and hydrated NAM, a thin zone of melting is illustrated at the top of the hydrated channel where the white region indicates melting > 1%; (D) viscosity structure corresponding to panel c, showing the marked decrease in viscosity of the solid matrix due to water-weakening from hydration of nominally anhydrous olivine; (E) As the calculation continues, advection of the slab-adjacent wedge peridotite results in the development of a hydrated channel, bounded at the top by a thin melt lens. The solid flow streamlines shows a marked change in trajectory upon impacting the hydrated channel, with an increasing upward component; (F) The hydrated channel is defined by high concentrations of water in NAM (olivine up to ~1400 ppm, clinopyroxene up to ~5700 ppm, orthopyroxene up to ~2800 ppm, and garnet up to ~600 ppm as the solubility of water in NAM increases with pressure), which influence the viscosity through the flow law, and result in the low-viscosity channel (LVC). The peak water content in NAMs in the LVC, as it reflects a water-saturated zone, is primarily a reflection of the solubility of water at a particular temperature and pressure, and therefore the peak hydration does not vary significantly among the models tested. Note that the contour interval of the stream function in the slab and descending mantle is twice the value in the wedge.

calculation, with the silicate liquid phase suppressed in pHMELTS, demonstrates (Fig. 3B). If melting is not present within the wedge, for whatever reason, then a low-viscosity "wedge" geometry may prevail. In areas with closely spaced slab dehydration reactions, the melting region is oriented at a slight angle to the slab–wedge interface, as progressive depletion of the advecting slab-adjacent mantle displaces the water-saturated solidus towards higher temperatures, further into the wedge. Melting results in net cooling of the residue before it turns
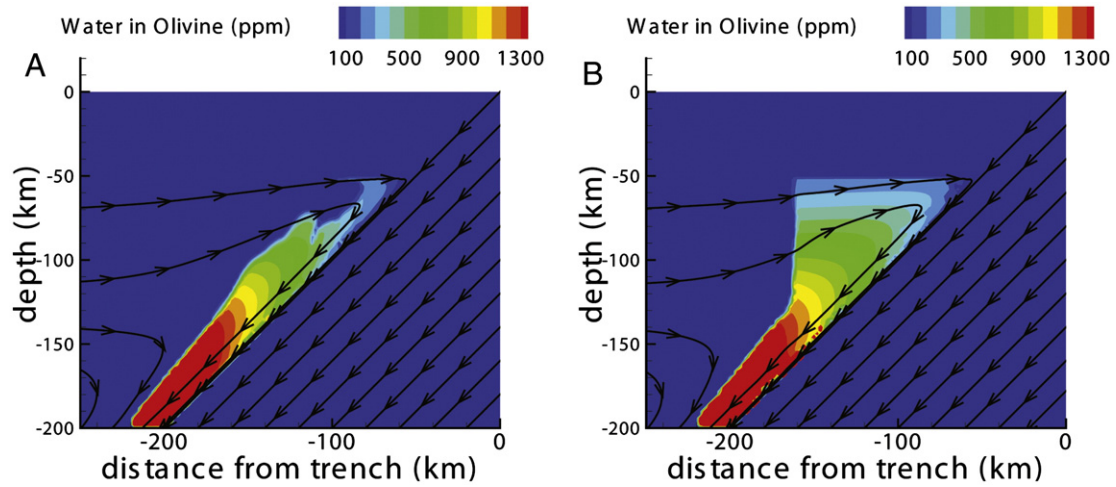
Fig. 3. (A) Water in olivine (which defines the LVC) (B) An experiment with melting suppressed within the pHMELTS model, to test the impact of melting as the primary restriction on the thickness of the LVC. Note that the contour interval of the stream function in the slab and descending mantle is twice the value in the wedge. A sharp, upper boundary is imposed to prevent water from entering low-temperature and low-pressure regions where pHMELTS is not stable. The sharp edge along the left-hand side of the hydrated region denotes the vertical transport path of fluid from the deepest dehydration reaction within the slab. As melting is suppressed, there is no upper boundary on the low-viscosity zone.
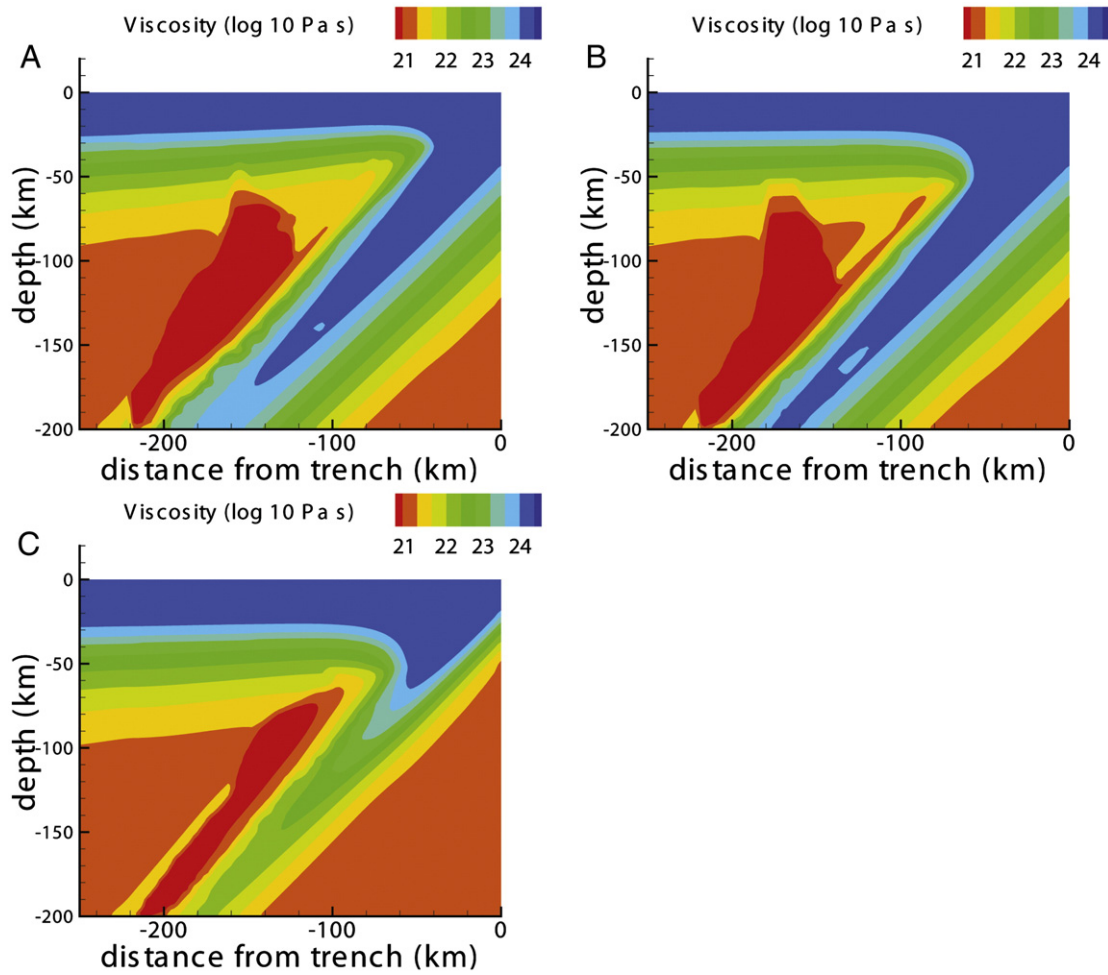

Fig. 4. Influence of slab age and convergence velocity on the development of the LVC as shown by the resulting viscosity structure. Models with a 45° slab dip are compared, arranged such that the effects of increasing slab age and increasing slab convergence velocity can be evaluated at constant slab dip angle. Fig. 4A (NIB) and b (ADD1) represent the subduction of old, cold slabs (thermal age 135 Ma), differentiated primarily by slow (50 mm/yr) and fast (87 mm/yr) convergence velocity. Fig. 4C (ADD2) represents the subduction of a young, warm slab (thermal age 18 Ma), with slower velocity (Table 2). The abrupt truncations at the base of the LVC (Fig. 4A, B) at 220 km from the trench (x-axis) are due to a change in particle distribution (Fig. 1A) and the upper limit of fluid migration (Fig. 4B) is imposed by the position of the overlying lithosphere.

the corner in the wedge, potentially counteracting the effect of the temperature-dependent viscosity, which otherwise allows for higher slab-adjacent temperatures than an isoviscous rheology (Peacock et al., 2005). We do not observe decompression melting resulting from the change in the flow field as a result of LVC development.

3.2. Model comparison (Table 2)

Models involving young slabs show thin, uniform LVCs (Fig. 4C, Fig. 2f). Cases involving older slabs instead have LVCs that are very thin at shallow depths, increase in thickness dramatically around 100–150 km depth, and gradually thin towards 200 km depth as hydrated material is advected out of the model domain (Fig. 4A, B). The thick hydrated envelope above older, colder slabs originates from stronger fluid sources at greater depths whereas models with young, warm slabs rely on fluid sources from the slab at <130 km depth. In regions of high water flux (high φ) at higher pressures, which occur above older slabs, the melting column is longer, and time-dependent cooling of the wedge occurs. This results in an upward retreat of the water-saturated solidus and an extension of the fluid pathways, allowing fluids from serpentinite to interact with a shallow melting region (Fig. 7). Eventually, the zone of melting stalls below the thermal lithosphere, reducing to direct fluid transport into the overlying lithosphere (similar to the water transport columns of Iwamori, 1998) with melting restricted to the edges of the hydrated region (Fig. 6). The differences in LVC shape among the models with equal slab age can be attributed to slab velocity variations. Increasing convergence velocity

with other parameters held relatively constant results in a colder thermal regime, changing the locations of dehydration reactions within the slab. For younger slabs, there is melting at 100 km depth in both models, where lithospheric serpentinite dehydrates, but additional releases at lower pressures (50 mm/yr convergence) and at higher pressures (87 mm/yr convergence) determine the overall shape of the LVC. The model with more rapid convergence has a slightly thicker LVC due to the deeper fluid release. The slower converging case involves a greater lateral viscosity contrast between the ambient nominally anhydrous mantle wedge and the thinner LVC. The overall thinning at higher pressures is a result of the continuation of the LVC solely by advection of hydrated material down-dip, without strong additional fluid sources. For more mature slab models, higher convergence velocity likewise yields a slightly deeper fluid source and a somewhat thicker LVC at the base of the model domain. Notably, this is reflected in the position of the melting region (Fig. 6), which is further down-dip for the faster converging case.

Slab dip has a major control on the geometry of wedge hydration (Fig. 5). A shallowing dip angle results in a persistent uniform LVC of increased thickness. For steepening slab dips, the fluid pathways become closer to slab-parallel, resulting in a sharp thinning of the LVC at 200 km depth and large lateral variations in viscosity; overprinting of the cold boundary layer adjacent to the slab is not as extensive as in other models. The melting region is closer to the trench, reflecting a narrower trench-perpendicular region of fluid influx. The locations of fluid release in all models remain relatively constant throughout the experiment, except for the initial transient.
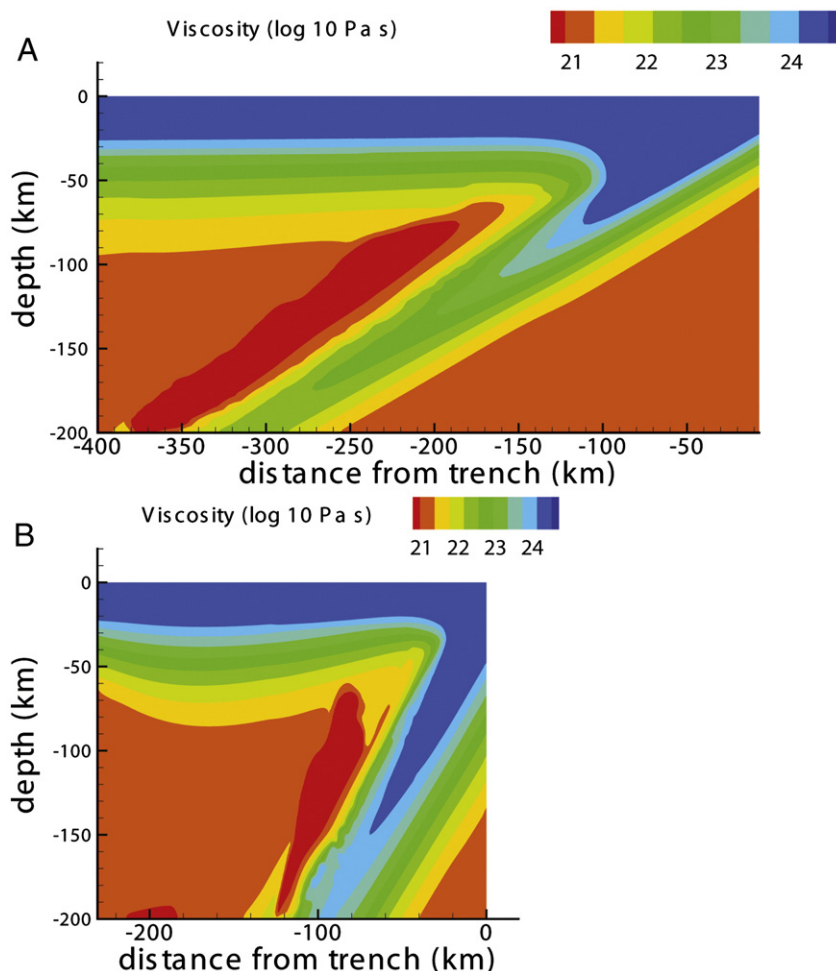

Fig. 5. Influence of the impact of changing slab dip on the geometry of the LVC. (A) SCR: slab dip shallowed to 30°. (B) NMAR: slab dip steepened to 60°.
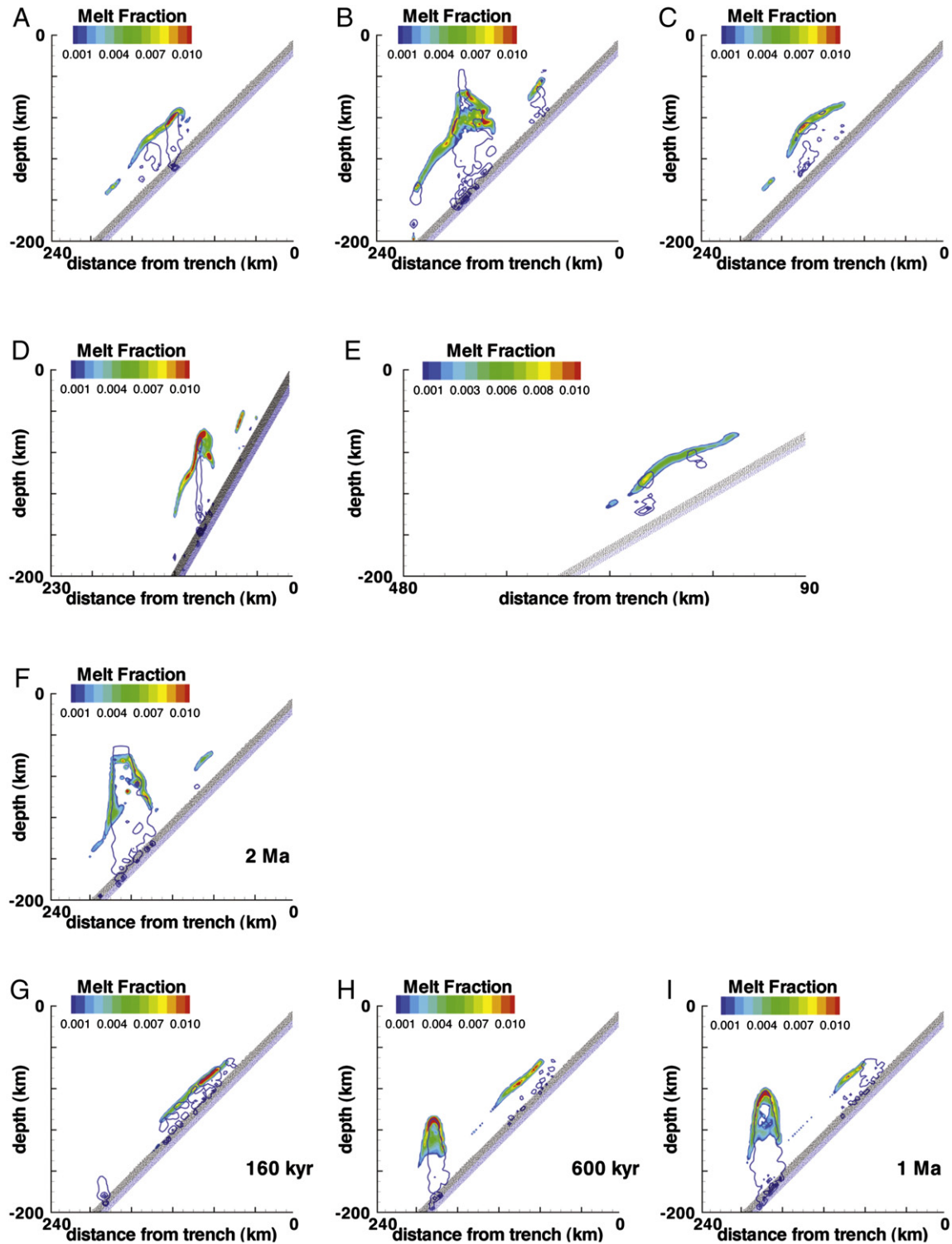
Fig. 6. Instantaneous melt fraction (color) and fluid release from the slab (blue contours), showing that melting is generally restricted to a thin (~6 km) lens immediately above fluid release locations within the slab. (A) CCR, (B) NIB, (C) ADD2, (D) NMAR, (E) SCR, (F) ADD1, (G–I) illustrate the evolution of the melting region and the changing fluid release locations over time for model ADD1.

Instantaneous melt fractions in all cases are low (<1%) (Fig. 6) as a consequence of the small time-step between extractions. However, using residual compatible trace element abundances to map cumulative melt fraction results in total melt fractions of up to 20% within the localized melting regions bounding the LVC, comparable to petrological estimates from arc magmas. The influence of the latent heat of melting on the thermal regime (and slight additional cooling due to interpolation-related numerical diffusion) is to thicken the LVC

(Fig. 6G–I). The displacement of the solidus could be exaggerated by prior depletion, which would result in even thicker LVCs.

Our models are restricted in vertical dimension by the pressure limitations of pHMELTS, but the hydrated layer persists to the base of our model domain, and we can reasonably assume that it continues deeper. The increasing solubility of water in olivine with pressure may allow for an even greater influence on viscosity with depth, assuming that the slab has not been completely dehydrated. Indeed, for older

slab models, the serpentinite layer still contains as much as 6.8 wt.% H_2O as it exits the model domain.

3.3. Variation of fluid migration parameters

The range of φ encountered in the models results in variable fluid velocities (Table 2 caption). However, the largest source of uncertainty comes from estimates of η_W in Eq. (6) and there is a clear range of fluid transport behaviors dependent on the choice of d_m and η_W. The range in η_W reflects a variation in the H_2O content of supercritical fluids from ~25% to 100% at 800 °C (Audetat and Keppler, 2004). For lower values of η_W (0.01–0.1 Pa s), the fluid moves so rapidly that the model time step is inadequate to describe its interaction with the solid. Some fluid whose velocity is low because φ is small reacts to give a water-undersaturated LVC with geometry similar to that described above (not shown). For higher values of η_W (~1.0 Pa s), the majority of the fluid moves vertically ~10^{-8} m/s, resulting in the water-saturated hydration structures described above. A very small proportion of fluids remains at low φ within the LVC and is advected down-dip. In general, however, the amount of fluid downwelling is smaller than observed by Cagnioncle et al. (2007) for a given set of parameters. Additional fluids associated with high φ are observed moving rapidly through the system with little interaction (for η_W ~ 1.0 Pa s). The persistence of a localized low-viscosity region over a range of η_W and φ is significant. Whilst the parameters resulting in the stable, water-saturated LVC may be considered extreme (η_W=1.0 Pa s, d_m=0.001 m), this could be a consequence of the choice of timestep. Following standard procedure, ConMan uses the Courant timestep, which maximizes step size while preserving numerical stability, but that may be inappropriate for modeling reactive hydrous transport. To approach near-equilibrium fluid transport for η_W=0.1, say, would require a timestep at least 10× smaller and this would be computationally expensive. Instead, we use η_W=1.0 Pa s in the models presented here and note that at pressures above the second critical end-point (Mibe et al., 2007) this viscosity may be quite reasonable.

4. Discussion

4.1. The low-viscosity channel (LVC)

In all models we observe the development of a continuous localized region of hydrous phases and hydrated NAM along the slab-mantle interface. This region extends upward from the slab-wedge interface sometimes as far as the overlying lithosphere, up to 100 km in some cases. Water-weakening results in a large viscosity reduction (10^1 to 10^2 ×), defining an LVC. The geometry of the LVC is related to (i) the distribution and flux of fluid resulting from slab dehydration reactions, (ii) melting (cooling and prior melt depletion due to flux melting or to potential back-arc spreading), and (iii) the slab dip angle. Slab thermal age and dip angle exert primary controls over the geometry and viscosity of the LVC and hence the degree of viscous decoupling along the slab-wedge interface. Convergence velocity exerts a secondary control, mainly affecting LVC shape and position of the melting region. Steeper-dipping slabs (>45°) imply melting regions closer to the trench. Subduction of older slabs preferentially samples shallow melts from deeper fluid sources. Shallower dipping and younger slabs emphasize melts from shallower fluid sources. The different fluid-mobile trace element chemistries of AOC and serpentinized lithosphere should, therefore, be reflected in the trace element patterns of arc lavas from different regions (Hebert et al., in prep) (Fig. 7). Additionally, the more extensive low-viscosity region in models with older slabs has a significant impact on the force balance, manifesting itself in geophysical observables such as the geoid, gravity, and topography and allowing prediction of LVC shape beneath different subduction systems (Hebert and Gurnis, in press).

Unlike Gerya and Yuen (2003), we do not see Rayleigh–Taylor instabilities along the surface of the hydrated LVC because of the lower density contrasts across that boundary predicted by our models. We do not include a very low-density sediment layer or allow mechanical (solid) mixing between slab lithologies and mantle wedge peridotite (which would decrease the density of the hydrated peridotite relative to the anhydrous peridotite above it). Additionally, we do not observe serpentinized wedge peridotite juxtaposed against ambient nominally anhydrous peridotite; there is always some distance between the stability limit of the hydrous phases and the pHMELTS-calculated water-saturated peridotite solidus, leading to lower density contrasts in our models. There is residual amphibole present in the shallowest melt source regions, but along the majority of the slab surface, chlorite is the only stable hydrous phase and is restricted to within ~ 10 km of the slab surface. The slight density increase associated with the sharp drop in water content along the top of the LVC boundary ($\Delta\rho$ ~20–50 kg/m^3) is much less than that predicted by Gerya and Yuen (2003) for the potential diapir-source region along the top of the slab.

Iwamori (1998) presents a numerical model that describes the generation and migration of fluids from the slab and their consequent equilibration with the overlying convecting mantle solids. Similar to our results, there is a stable slab-adjacent layer of chlorite within the wedge and a displacement of the melting region into the wedge. Iwamori's (1998) chlorite layer absorbs the majority of slab-derived water and subsequent dehydration of chlorite around 150 km depth gives a single fluid source, transporting water to the melting region (Iwamori, 1998). Our model, even though it includes water partitioning into NAM, yields fluid flux sufficient to saturate both the slab-adjacent layer of chlorite and an overlying thickness of NAM. Successive fluid flux through this saturated zone produces melting at multiple depths within the wedge, ultimately producing a slab-parallel melting region displaced into the wedge. Our melting region looks very similar to the disequilibrium transport case of Iwamori (1998), in which water is allowed to "leak" from the slab-adjacent hydrated layer above 150 km depth.

Independent of results presented here, time-dependent models of subduction show that slab dip can be substantially influenced by a LVC
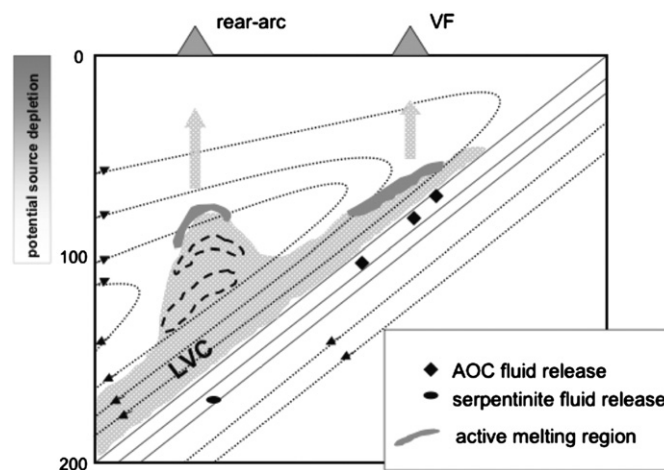

Fig. 7. Schematic of the low-viscosity channel (LVC) geometry, including hydrous melt layer for the NIB model case. Dehydration reactions in the down-going slab release water, which rises into the overlying mantle wedge and reacts with peridotite to form hydrous phases and to hydrate NAM. Locations of water release from slab dehydration reactions showing the discontinuous nature of the water release due to crossing of reaction boundaries. The shallower dehydration reactions are due to reaction boundaries in the AOC while the deeper reactions are in the lithospheric serpentinite layer. Once saturated, water can rise through the hydrated NAM layer into the hotter regions of the wedge, where it induces water-fluxed melting. Excluding hydrous phases, and assuming a peridotite assemblage of 57% olivine, 8% garnet, 16% orthopyroxene, and 16% clinopyroxene, the LVC can potentially transport ~2200 ppm H_2O into the deeper mantle in NAM alone, providing a significant, robust, water source.

with a thickness of tens of kilometers and a parameterized viscosity contrast of a factor of two (Manea and Gurnis, 2007). In such models, an LVC generally leads to increasing slab dips as the suction force drawing the slab upward is reduced. Our model provides a self-consistent mechanism to generate such an LVC geometry. We are unable to demonstrate the effect of changing slab dip on an existing LVC with our kinematic slab model, but we can make estimates based on our results encompassing a range of slab dip angles. Initiation of subduction at shallow dip angle would result in a continuous LVC to at least 200 km depth of roughly uniform thickness. If slab dip increases as a result (Manea and Gurnis, 2007), the LVC would most likely remain as a continuous channel but the thickness may change and, more importantly, the positions of the melting regions within the wedge would change. This may lead to observable increases in lava flux from the volcanic front as melt production migrates from the rear-arc (Fig. 7) towards the trench with increasing slab dip. The trenchward progression could also be mapped by signals in fluid-mobile trace elements specific to serpentinite dehydration proceeding from the rear-arc to the volcanic front with time.

4.2. Water mobility: recycling to deep mantle and timing of transport to active melting region

The formation of enriched mid-ocean-ridge basalts (E-MORB) at normal mid-ocean ridges requires chemical heterogeneities in the mantle, possibly generated by recycling at subduction zones (Schmidt and Poli, 1998; Dixon et al., 2002; Le Roux et al., 2002; Cooper et al., 2004; Donnelly et al., 2004). Geochemical arguments exist for the relative importance of the slab-adjacent mantle, metasomatized by either slab-derived fluids or small-degree slab melts, rather than recycled AOC or sediments themselves (Cooper et al., 2004; Donnelly et al., 2004). Analyses of basaltic glasses from the mid-Atlantic ridge near the Azores reveal evidence (high $\delta^{18}O$, La/Sm, Ce/Pb, and $^{87}Sr/^{86}Sr$ and low $^{143}Nd/^{144}Nd$) for an enriching agent (Cooper et al., 2004). Additionally, high lithium isotope ratios in enriched East Pacific Rise lavas may be explained by enrichment by fluid-modified recycled wedge material instead of AOC (Elliott et al., 2006). The slab-adjacent mantle is carried down with the subducting slab, but may be more efficiently mixed in with ambient upper mantle than AOC, producing enriched source regions for normal upwelling and melting beneath ridges. In our models, the LVC emerges as a stable zone of fluid-modified slab-adjacent mantle material and trapped low-degree melts that is transported with the slab-dominated flow field, presumably to depths beyond our model region, where it may, at some point, separate from denser oceanic crust and mix with surrounding upper mantle material. As the subducting slab descends, the pressure-temperature path of the LVC will not cross the solidus, providing a mechanism for the recycling of water and slab-adjacent water-rich wedge material deep into the mantle.

The presence of the LVC has implications for the timing of fluid-bearing element transport from the slab to the arc. It has been hypothesized that two separate mantle wedge enrichment mechanisms result in the ^{238}U excesses observed at the Mariana arc: an episode of sediment-derived (uranium-rich) fluid addition to the mantle source followed by >350 kyr of radiogenic ingrowth as the solid flow advects the material deeper, and then a second episode of fluid influx from the dehydrating AOC (Elliott et al., 1997). The interval from this second release of fluid to the eruption of lavas, which necessarily includes melt migration and lower crustal processing, is on the order of tens of thousands of years, suggesting that the fluids themselves are the trigger for initiation of mantle wedge melting (Elliott et al., 1997). The LVC, defined by tens of kilometers of water-saturated mantle material, may allow fairly rapid fluid transport with minimal chemical water-rock equilibration resulting in direct delivery to the melting region and immediate triggering of melting. Neither the chlorite-breakdown mechanism of Iwamori (1998) nor the amphibole-break-

down mechanism of Davies and Stevenson (1991) is able to deliver fluids so rapidly to the melting regime. In this sense the occurrence of a water-saturated LVC in the present model is a critical element in the development of a physical picture of subduction that satisfies geochemical and geochronological constraints.

4.3. Melting

In all models, there is a distinct region of melt production within the mantle wedge. The dominant factor in subduction systems controlling this spatial distribution appears to be the amount and location of fluid release within the slab. We do not account for the influence of any melt lens on viscosity in our models but it could serve either to increase the effective thickness of the LVC, or to smooth the viscosity transition from the LVC into the interior of the mantle wedge. In contrast to our near-fractional melt extraction scheme, melt migration at depths greater >90 km may be consistent with porous/reactive flow (Nakajima et al., 2005), providing an additional transport mechanism for water. Allowing hydrous melts to react with solids during migration will redistribute water within NAM beyond the LVC, leading to a finite extension of the hydration region, smoothly decreasing water activity, and a wedge-type low-viscosity geometry.

A number of geochemical and petrological studies have suggested that partial melting of subducting slab components (sediment and/or AOC) is a possibility in many arc systems. Evidence includes recycling of trace elements, such as Th, that are relatively fluid-immobile but can be strongly partitioned into partial melts of metasediments and metabasalt (Plank and Langmuir, 1993; Elliott et al., 1997; Plank and Langmuir, 1998; Johnson and Plank, 1999), and similarities between trace element patterns of partial melts of eclogite and primitive arc andesites (Yogodzinski and Kelemen, 1998; Defant and Kepezhinskas, 2001; Yogodzinski et al., 2001; Grove et al., 2002; Tatsumi et al., 2001). Comparison with the water-saturated MORB solidus of Hacker et al. (2003) (i.e., 650–700 °C from 1–3 GPa) shows that we would not reasonably expect melting of AOC for the *PT* conditions of any of our models (Fig. 8). If, indeed, melting of the slab were to occur, it would encourage partitioning of water into the melt phase and reduce the capacity of fluid for transport into the wedge and initiation of melting, with implications for the development of the LVC. Instead, migration of the hydrous slab melts would be the main transport mechanism for water, with a more complicated fluxing process to initiate peridotite melting.

We note that the volcanic front forming at nearly constant height (~100 km) above the Wadati–Benioff zone does not appear to be fulfilled by a melt lens that extends along the slab surface. However, Syracuse and Abers (2006) demonstrated that the depth from the slab to the volcanic center can range from 72 to 173 km, with the global average being ~105 km. We do not account for melt migration processes that may serve to focus the melt (Spiegelman and McKenzie, 1987; Furukawa, 1993; Hall and Kincaid, 2001), or may exploit the channel geometry for flow reversals back up the slab. Despite this shortcoming, we can infer quite a lot from the positions of zones of active melting. Seismic tomographic studies in northeastern Japan show a low-velocity and high-attenuation zone in the mantle wedge, sub-parallel to the slab (Zhao, 2001; Hasegawa et al., 2005). These discontinuous regions exist at depths less than 150 km, are separated from the upper surface of the slab by ~50 km, and show very similar geometries to melting regions calculated by GyPSM-S, inclined towards the position of the arc.

Latent heat of melting appears to be the cause of the significant cooling of the mantle wedge. Since we remove melt completely from the system (above a certain porosity), we do not allow for crystallization of that melt within the overlying lithosphere, which may counteract wedge cooling. At pressures less than 1 GPa, pHMELTS predicts lower solidus temperatures than Grove et al. (2006), while at higher pressures it gives significantly higher temperatures with a
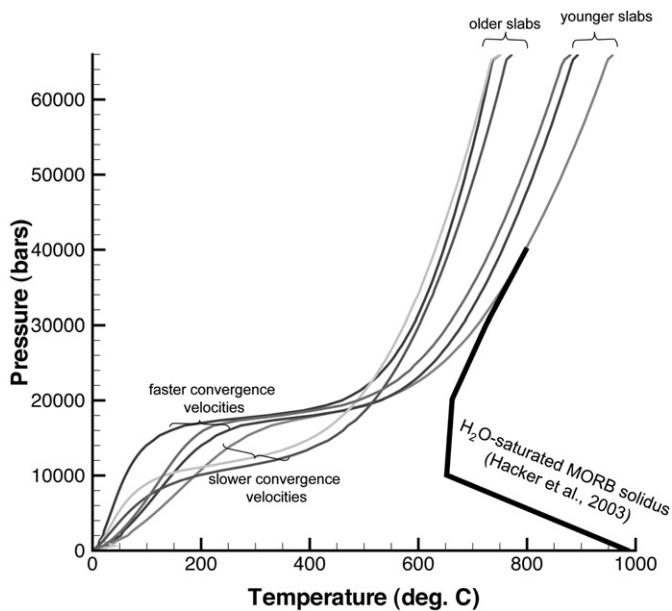
Fig. 8. Pressure–temperature trajectories of the slab–wedge interface for the six models with the water-saturated MORB solidus from Hacker et al., 2003. We neglect slab melting in our models, which refers to melting of the altered oceanic crust, as sediments are not included. The only model that approaches the water-saturated MORB solidus is ADD2, around 4.0 GPa.

steeper dT/dP solidus curve, (1150 °C vs. 800–1000 °C at 3 GPa). This systematic offset may be responsible for an over-extension of the zone of active melting into the wedge (especially above 3 GPa) and/or the lack of coexisting chlorite and melt in our models. However, the overall relationship between fluid migration, hydration of NAM, and displacement of the inclined zone of melting away from the slab with increasing pressure should be robust.

4.4. Impact of LVC on seismic wave propagation

Seismic velocity and attenuation studies have interpreted a hydrated region directly adjacent to the slab. From regionally detected body-wave phases, above seismically fast slabs there are low velocity layers (LVLs) with thicknesses of 5–10 km in the Mariana, Japan (Chen et al., 2007), Kurile, Nicaragua (Abers et al., 2003), and Aleutian arcs, and up to 20 km in parts of Alaska (Ferris et al., 2003). Results for Japan suggest a LVL extending to 300 km depth with substantial velocity reduction. The P-wave velocity reduction could be as much as 14% if the thickness of the LVL is only 10 km, but only 4% if the layer is 30 km thick (Chen et al., 2007), suggesting a thick zone of hydrated phases. In addition, studies of seismic attenuation (with lower spatial resolution than the velocity models) show broad zones of high attenuation (low Q) above slabs in Tonga (Roth et al., 2000), Alaska (Stachnik et al., 2004), and elsewhere.

The presence of hydrous phases can have a direct impact on seismic properties, so a continuous layer of hydrous phases along the slab–wedge interface has been hypothesized to explain low-velocity anomalies in subduction zones (Ferris et al., 2003; Kawakatsu and Watada, 2007). While hydrous phases can certainly hold more water than NAM, it remains true that NAM can account for significant amounts of water (e.g., as much as 0.6–0.9 wt.% in olivine alone at 12 GPa (Mosenfelder et al., 2006; Smyth et al., 2006)) and, with water solubility increasing steadily with increasing pressure, they may have an indirect effect on seismic properties. The LVC is defined by high water content in NAM, which can enhance anelasticity, increase attenuation and reduce seismic wave velocities (Karato et al., 1986; Karato and Jung, 1998; Mei and Kohlstedt, 2000; Karato, 2003). Therefore, a continuous channel of high water content in NAM may be

consistent with regionally detected body-wave phase results showing low velocity layers (LVLs) tens of kilometers thick above slabs (Chen et al., 2007).

5. Conclusions

As our models show, an integrated self-consistent subduction zone model is essential to demonstrate certain behaviors, such as the development of boundary features along the slab–wedge interface, and to simultaneously explain geophysical and geochemical observations. The low-viscosity region of the wedge may be a large-scale volume extending from the slab–mantle interface to the back-arc (e.g. Billen and Gurnis, 2001) or a relatively thin, continuous channel defined by water-saturated NAM and hydrous phases along the slab–mantle interface, depending on subduction parameters (slab age, convergence velocity, slab dip angle). The LVC is a consequence of the migration of fluids into the mantle wedge and reaction with peridotite to produce hydrous phases and higher water contents in NAM. Its extent is limited by the onset of melting and is therefore dependent on the position of the water-saturated solidus, which depends on source depletion (prior melt extraction) and the thermal evolution of the wedge. The zone of active melting exists at the upper surface of the LVC, and the thickness and instantaneous melt fraction are restricted in our models by the assumption of near-fractional melt extraction and the limitation of water transport to the hydrous fluid phase. Despite varying subduction parameters, the geometries of the melting regions are quite similar in all models: discontinuous lenses inclined to the slab surface and displaced from it by tens of kilometers. Fluid flux from the slab is found to be sufficient to saturate both hydrous minerals and NAM in the LVC, allowing direct and rapid vertical transport of subsequent slab fluids to the region of melting, eliminating the need for a slow slab-coupled advection step to move fluids away from the cold slab. The persistence of the LVC provides mechanism by which hydrated slab-adjacent mantle material (potentially a significant reservoir of water and very low-degree mantle melts) is transported to the deep mantle without melting, providing a source for enriched OIB magmas such as the Azores. The LVC is also significant for its effect on the large-scale flow field within the wedge, including possible slab decoupling (Billen and Gurnis, 2001) and changes in slab dip (Manea and Gurnis, 2007). Additional evidence for the existence of the LVC includes seismic wave propagation and attenuation, with recent studies showing the significant displacement of the active melting region from the slab–wedge interface (Zhao, 2001; Hasegawa et al., 2005).

References

Abers, G.A., Plank, T., Hacker, B.R., 2003. The wet Nicaraguan slab. Geophys. Res. Lett. 30 (2), 1098. http://dx.doi.org/10.1029/2002GL015649.
Arcay, D., Tric, E., Doin, M.-P., 2005. Numerical simulations of subduction zones: effect of slab dehydration in the mantle wedge dynamics. Phys. Earth Planet. Inter. 149, 133–153.
Asimow, P.D., Dixon, J.E., Langmuir, C.H., 2004. A hydrous melting and fractionation model for mid-ocean ridge basalts: application to the Mid-Atlantic Ridge near the Azores. Geochem. Geophys. Geosyst. 5 (1), Q01E16. doi:10.1029/2003GC000568.
Audetat, A., Keppler, H., 2004. Viscosity of fluids in subduction zones. Science 303, 513–516.

Batchelor, G.K., 1967. An Introduction to Fluid Dynamics. Cambridge University Press.

Berman, R.G., 1988. Internally consistent thermodynamic data for minerals in the system $Na_2O–K_2O–CaO–MgO–FeO–Fe_2O_3–Al_2O_3–SiO_2–TiO_2–H_2O–CO_2$: representation, estimation, and high temperature extrapolations. J. Petrol. 89, 168–183.

Billen, M.I., Gurnis, M., 2001. A low viscosity wedge in subduction zones. Earth Planet. Sci. Lett. 193, 227–236.

Brooks, A.N., Hughes, T.R.J., 1982. Streamline upwind Petrov–Galerkin formulations for convection dominated flows with particular emphasis on the incompressible Navier–Stokes equations. Comput. Methods Appl. Mech. Eng. 32 (1–3), 199–259.

Cagnioncle, A.-M., Parmentier, E.M., Elkins-Tanton, L., 2007. Effect of solid flow above a subducting slab on water distribution and melting at convergent plate boundaries. J. Geophys. Res. 112, B09402. doi:10.1029/2007/JB004934.

Chen, M., Tromp, J., Helmburger, D., Kanamori, D., 2007. Waveform modeling of the slab beneath Japan. J. Geophys. Res. Solid Earth 112, B02305. doi:10.1029/2006JB004394.

Cooper, K.M., Eiler, J.M., Asimow, P.D., Langmuir, C.H., 2004. Oxygen isotope evidence for the origin of enriched mantle beneath the mid-Atlantic ridge. Earth Planet. Sci. Lett. 220, 297–316.

Davies, J.H., Stevenson, D.J., 1991. Physical model of source region of subduction zone volcanics. J. Geophys. Res. 97 (B2), 2037–2070.

Defant, M.J., Kepezhinskas, P., 2001. Evidence suggests slab melting in arc magmas. EOS 82, 65–69.

Donnelly, K.E., Goldstein, S.L., Langmuir, C.H., Spiegelman, M., 2004. Origin of enriched ocean ridge basalts and implications for mantle dynamics. Earth Planet. Sci. Lett. 226, 347–366.

Dixon, J.E., Leist, L., Langmuir, C.H., Schilling, J.-G., 2002. Recycled dehydrated lithosphere observed in plume-influenced mid-ocean-ridge basalt. Nature 420, 385–389.

Elliott, T., Plank, T., Zindler, A., White, W., Bourdon, B., 1997. Element transport from slab to volcanic front at the Mariana arc. J. Geophys. Res. 102 (B7), 14991–15019.

Elliott, T., Thomas, A., Jeffcoate, A., Niu, Y., 2006. Lithium isotope evidence for subduction-enriched mantle in the source of mid-ocean-ridge basalts. Nature 443 (5), 565–568. http://dx.doi.org/10.1038/nature05144.

Ferris, A., Abers, G.A., Christensen, D.H., Veenstra, E., 2003. High-resolution image of the subducted Pacific plate beneath central Alaska, 50–150 km depth. Earth Planet. Sci. Lett. 214 (3–4), 575–588. http://dx.doi.org/10.1016/S0012-821X(03)00403-5.

Furukawa, F., 1993. Magmatic processes under arcs and formation of the volcanic front. J. Geophys. Res. 98, 8309–8319.

Ghiorso, M.S., Sack, R.O., 1995. Chemical mass transfer in magmatic processes; IV, A revised and internally consistent thermodynamic model for the interpolation and extrapolation of liquid–solid equilibrium magmatic systems at elevated temperatures and pressures. Contrib. Mineral. Petrol. 119 (2–3), 197–212.

Ghiorso, M.S., Hirschmann, M.M., Reiners, P.W., Cress, V.C., 2002. The pMELTS: a revision of MELTS from improved calculation of phase relations and major element partitioning related to partial melting of the mantle to 3 GPa. Geochem. Geophys. Geosyst. 3. doi:10.1029/2001GC000217.

Gerya, T.V., Yuen, D.A., 2003. Rayleigh–Taylor instabilities from hydration and melting propel 'cold plumes' at subduction zones. Earth Planet. Sci. Lett. 212, 47–62.

Grove, T.L., Parman, S.W., Bowring, S.A., Price, R.C., Baker, M.B., 2002. The role of an H_2O-rich fluid component in the generation of primitive basaltic andesites and andesites from the Mt. Shasta region, N. California. Contrib. Mineral. Petrol. 142 (4), 375–396.

Grove, T.L., Chatterjee, N., Parman, S.W., Médard, E., 2006. The influence of H_2O on mantle wedge melting. Earth Planet. Sci. Lett. 249, 74–89.

Hacker, B.R., Abers, G.A., 2004. Subduction factory III: an excel worksheet and macro for calculating the densities, seismic wave speeds, and H_2O contents of minerals and rocks at pressure and temperature. Geochem. Geophys. Geosyst. 5. doi:10.1029/2003GC000614.

Hacker, B.R., Abers, G.A., Peacock, S.M., 2003. Subduction factory-1. Theoretical mineralogy, densities, seismic wave speeds, and H_2O contents. J. Geophys. Res. Solid Earth 108 (B1). http://dx.doi.org/10.1029/2001JB001129.

Hall, P., Kincaid, C., 2001. Diapiric flow at subduction zones: a recipe for rapid transport. Science 292, 2472–2475.

Hasegawa, A., Zhao, D., Hori, S., Yamamoto, A., Horiuchi, S., 2005. Deep structure of the northeastern Japan arc and its implications for crustal deformation and shallow seismic activity. Tectonophysics 403, 59–75.

Hauri, E.H., Gaetani, G.A., Green, T.H., 2006. Partitioning of water during melting of the Earth's upper mantle at H_2O-undersaturated conditions. Earth Planet. Sci. Lett. 248, 715–734.

Hebert, L.B., Gurnis, M., in press. The Island Arc. Geophysical Implications of Izu-Bonin Mantle Wedge Hydration from Chemical Geodynamic Modeling.

Hirth, G., Kohlstedt, D.L., 1996. Water in the oceanic upper mantle; implications for rheology, melt extraction, and the evolution of the lithosphere. Earth Planet. Sci. Lett. 144 (1–2), 93–108.

Hirth, G., Kohlstedt, D.L., 2003. Rheology of the upper mantle and the mantle wedge: a view from the experimentalists. In: Eiler, J. (Ed.), Geophysical Monograph, vol. 138, pp. 83–105.

Iwamori, H., 1998. Transportation of H_2O and melting in subduction zones. Earth Planet. Sci. Lett. 160, 65–80.

Johnson, M.C., Plank, T., 1999. Dehydration and melting experiments constrain the fate of subducted sediments. Geochem. Geophys. Geosyst. 1 1999GC000014.

Karato, S., 2003. Mapping water content in the upper mantle. In: Eiler, J. (Ed.), Geophysical Monograph, vol. 138, pp. 135–152.

Karato, S., Jung, H., 1998. Water, partial melting, and the origin of the seismic low velocity and high attenuation zone in the upper mantle. Earth Planet. Sci. Lett. 157 (3–4), 193–207.

Karato, S., Paterson, M.S., Fitzgerald, J.D., 1986. Rheology of synthetic olivine aggregates: influence of grain size and water. J. Geophys. Res. 91, 8151–8176.

Kawakatsu, H., Watada, S., 2007. Seismic evidence for deep-water transportation in the mantle. Science 316, 1468–1471.

King, S.D., Raefsky, A., Hager, B.H., 1990. ConMan: vectorizing a finite element code for incompressible two-dimensional convection in the Earth's mantle. Phys. Earth Planet. Inter. 59 (3), 195–207.

Le Roux, P.J., le Roux, A.P., Schilling, J.G., Shimizu, N., Perkins, W.W., Pearce, N.J.G., 2002. Mantle heterogeneity beneath the southern Mid-Atlantic Ridge: trace element evidence for contamination of ambient asthenospheric mantle. Earth Planet. Sci. Lett. 203, 479–498.

Manea, V., Gurnis, M., 2007. Subduction zone evolution and low viscosity wedges and channels. Earth Planet. Sci. Lett. 264 (1–2), 22–45.

McKenzie, D.P., Bickle, M.J., 1988. The volume and composition of melt generated by extension of the lithosphere. J. Petrol. 29 (3), 625–679.

Mei, S., Kohlstedt, D.L., 2000. Influence of water on plastic deformation of olivine aggregates 2. Dislocation creep regime. J. Geophys. Res. 105 (21), 21471–21481.

Mibe, K., Kanzaki, M., Kawamoto, T., Matsukage, K., Fei, Y., Ono, S., 2007. Second critical endpoint in the peridotite-H_2O system. J. Geophys. Res. 112, B03201. doi:10.1029/2005JB004125.

Mosenfelder, J.L., Deligne, N.I., Asimow, P.D., Rossman, G.R., 2006. Hydrogen incorporation in olivine from 2–12 GPa. Am. Mineral. 91 (2), 285–294. http://dx.doi.org/10.2138/am.2006.1943.

Nakajima, J., Takei, Y., Hasegawa, A., 2005. Quantitative analysis of the inclined low-velocity zone in the mantle wedge of northeastern Japan: a systematic change of melt-filled pore shapes with depth and its implications for melt migration. Earth Planet. Sci. Lett. 234, 59–70.

Pawley, A., 2003. Chlorite stability in mantle peridotite: the reaction clinochlore+enstatite=forsterite+pyrope+H_2O. Contrib. Mineral. Petrol. 144, 449–456.

Peacock, S.M., 1990. Fluid processes in subduction zones. Science 248, 329–337.

Peacock, S.M., van Keken, P.E., Holloway, S.D., Hacker, B.R., Abers, G.A., Ferguson, R.L., 2005. Thermal structure of the Costa Rica–Nicaragua subduction zone. Phys. Earth Planet. Inter. 149 (1–2), 187–200.

Peate, D.W., Pearce, J.A., 1998. Causes of spatial compositional variations in Mariana arc lavas: Trace element evidence. Island Arc 7, 479–495.

Pitzer, K.S., Sterner, S.M., 1994. Equations of state valid continuously from zero to extreme pressures for H_2O and CO_2. J. Chem. Phys. 101 (4), 3111–3116.

Plank, T., Langmuir, C.H., 1993. Tracing trace elements from sediment input to volcanic output at subduction zones. Nature 362, 739–743.

Plank, T., Langmuir, C.H., 1998. The chemical composition of subducting sediment and its consequences for the crust and mantle. Chem. Geol. 145, 325–394.

Roth, E.G., Wiens, D.A., Zhao, D.P., 2000. An empirical relationship between seismic attenuation and velocity anomalies in the upper mantle. Geophys. Res. Lett. 27 (5), 601–604. http://dx.doi.org.10.1029/1999GL005418.

Rüpke, L.H., Phipps-Morgan, J., Hort, M., Connolly, J., 2002. Are regional variations in Central American arc lavas due to differing basaltic versus peridotitic slab sources of fluids? Geology 30 (11), 1035–1038.

Rüpke, L.H., Phipps-Morgan, J., Hort, M., Connolly, J., 2004. Serpentine and the subduction water cycle. Earth Planet. Sci. Lett. 223, 17–34.

Scambelluri, M., Muntener, O., Ottolini, L., Pettke, T.T., 2004. The fate of B, Cl, and Li in the subducted oceanic mantle and in the antigorite breakdown fluids. Earth Planet. Sci. Lett. 222, 217–234.

Schmidt, M.W., Poli, S., 1998. Experimentally-based water budgets for dehydrating slabs and consequences for arc magma generation. Earth Planet. Sci. Lett. 163, 361–379.

Sidorin, I., Gurnis, M., 1998. Geodynamically consistent seismic velocity predictions at the base of the mantle. In: Gurnis, M., Wysession, M., Knittle, E., Buffett, B. (Eds.), The Core Mantle Boundary Region. American Geophysical Union, Washington, D.C., pp. 209–230.

Sleep, N.H., 1975. Stress and flow beneath island arcs. Geophys. J. Int. 42, 827–857.

Smith, P.M., Asimow, P.D., 2005. Adiabat_1ph: a new public front-end to the MELTS, pMELTS, and pHMELTS models. Geochem. Geophys. Geosyst. 6 (2), Q02004. doi:10.1029/2004GC000816.

Smith, P.M., Hebert, L.B., Asimow, P.D., Gurnis, M., 2007. Coupled petrological and geodynamic models of mantle flow in subduction zones; the importance of chlorite in the emergence of a low-viscosity channel. Eos Trans. AGU 88 (52) Fall Meet. Suppl., Abstract V43D–1637.

Smyth, J.R., Frost, D.J., Nestola, F., Holl, C.M., Bromiley, G., 2006. Olivine hydration in the deep upper mantle: effects of temperature and silica activity. Geophys. Res. Lett. 33 (L15301). doi:10.1029/2006GL026194.

Spiegelman, M., McKenzie, D., 1987. Simple 2-D models for melt extraction at mid-ocean ridges and island arcs. Earth Planet. Sci. Lett. 83, 137–152.

Stachnik, J.C., Abers, G.A., Christensen, D.H., 2004. Seismic attenuation and mantle wedge temperatures in the Alaska subduction zone. J. Geophys. Res. Solid Earth 109 (B10). http://dx.doi.org/10.1029/2004JB003018.

Stern, R.J., Fouch, M.J., Klemperer, S.L., 2003. An overview of the Izu-Bonin mariana subduction factory. In: Eiler, J. (Ed.), Geophysical Monograph, vol. 138, pp. 175–222.

Syracuse, E.M., Abers, G.A., 2006. Global compilation of variations in slab depth beneath arc volcanoes and implications. Geochem. Geophys. Geosyst. 7 (5), Q05017. doi:10.1029/2005GC001045.

Tatsumi, Y., Eggins, S., 1995. Subduction Zone Magmatism. Blackwell, Cambridge.

Tatsumi, Y., Ishikawa, N., Anno, K., Ishizaka, K., Itaya, T., 2001. Tectonic setting of high-Mg andesite magmatism in the SW Japan Arc: K–Ar chronology of the Setouchi volcanic belt. Geophys. J. Int. 144 (3), 625–631.

Ulmer, P., Trommsdorf, V., 1995. Serpentine stability to mantle depths and subduction-related magmatism. Science 268, 858–861.

Van Keken, P.E., Kiefer, B., Peacock, S., 2002. High-resolution models of subduction zones: Implications for mineral dehydration reactions and the transport of water into the deep mantle. Geochem. Geophys. Geosyst. 3 (10), 1056. doi:10.1029/2001GC000256.

Wark, D.A., Williams, C.A., Watson, E.B., Price, J.D., 2003. Reassessment of pore shapes in microstructurally equilibrated rocks, with implications for permeability of the upper mantle. J. Geophys. Res. 108 (B1, 2050). doi:10.1029/2001JB001575.

Workman, R.K., Hart, S.R., 2005. Major and trace element composition of the depleted MORB mantle (DMM). Earth Planet. Sci. Lett. 231 (1–2), 53–72. http://dx.doi.org/10.1016/j.epsl.2004.12.005.

Yogodzinski, G.M., Kelemen, P.B., 1998. Slab melting in the Aleutians: implications of an ion probe study of clinopyroxene in primitive adakite and basalt. Earth Planet. Sci. Lett. 158, 53–65.

Yogodzinski, G.M., Lees, J.M., Churikova, T.G., Dorendorf, F., Woerner, G., Volynets, O.H., 2001. Geochemical evidence for the melting of subducting oceanic lithosphere at plate edges. Nature 409, 500–504.

Zhao, D.P., 2001. Seismological structure of subduction zones and its implications for arc magmatism and dynamics. Phys. Earth Planet. Inter. 127, 197–214.

Zimmerman, M.E., Zhang, S., Kohlstedt, D.L., Karato, S., 1999. Melt distribution in mantle rocks deformed in shear. Geophys. Res. Lett. 26 (10), 1505–1508.